



**UNIVERSITY OF LEEDS**

This is a repository copy of *A nutrient control on marine anoxia during the end-Permian mass extinction*.

White Rose Research Online URL for this paper:  
<http://eprints.whiterose.ac.uk/163093/>

Version: Accepted Version

---

**Article:**

Schobben, M, Foster, WJ, Sleveland, ARN et al. (8 more authors) (2020) A nutrient control on marine anoxia during the end-Permian mass extinction. *Nature Geoscience*, 13. pp. 640-646. ISSN 1752-0894

<https://doi.org/10.1038/s41561-020-0622-1>

---

**Reuse**

Items deposited in White Rose Research Online are protected by copyright, with all rights reserved unless indicated otherwise. They may be downloaded and/or printed for private study, or other acts as permitted by national copyright laws. The publisher or other rights holders may allow further reproduction and re-use of the full text version. This is indicated by the licence information on the White Rose Research Online record for the item.

**Takedown**

If you consider content in White Rose Research Online to be in breach of UK law, please notify us by emailing [eprints@whiterose.ac.uk](mailto:eprints@whiterose.ac.uk) including the URL of the record and the reason for the withdrawal request.



[eprints@whiterose.ac.uk](mailto:eprints@whiterose.ac.uk)  
<https://eprints.whiterose.ac.uk/>

1 **A nutrient control on marine anoxia during the end-Permian**  
2 **mass extinction**

3 Martin Schobben<sup>1,2</sup>, William J. Foster<sup>2,3</sup>, Arve R.N. Sleveland<sup>4</sup>, Valentin Zuchuat<sup>4</sup>, Henrik H.  
4 Svensen<sup>4</sup>, Sverre Planke<sup>4</sup>, David P.G. Bond<sup>5</sup>, Fons Marcelis<sup>6</sup>, Robert J. Newton<sup>1</sup>, Paul B.  
5 Wignall<sup>1</sup>, Simon W. Poulton<sup>1</sup>

---

<sup>1</sup> School of Earth and Environment, University of Leeds, Leeds, LS2 9JT, UK

<sup>2</sup> Museum für Naturkunde, Leibniz Institute for Research on Evolution and Biodiversity, 10115  
Berlin, Germany

<sup>3</sup> Universität Potsdam, Institute of Geosciences, Potsdam, Germany

<sup>4</sup> Centre for Earth Evolution and Dynamics (CEED), Department of Earth Sciences, University  
of Oslo, P.O. box 1028, Blindern, 0315 Oslo, Norway

<sup>5</sup> School of Environmental Sciences, University of Hull, Hull, HU6 7RX, UK

<sup>6</sup> Shell Global Solutions International B.V., Postbus 38000, 1030 BN Amsterdam, Netherlands

Oxygen deprivation and sulfide toxicity is considered a potent kill mechanism during the mass extinction just before the Permian–Triassic boundary (~251.9 million years ago). However, the mechanism that drove vast stretches of the ocean to an anoxic state is unclear. Here, we present paleoredox and phosphorus speciation data for a marine bathymetric transect from Svalbard. This shows that, prior to the extinction, enhanced weathering driven by Siberian Traps volcanism increased the influx of phosphorus, thus enhancing marine primary productivity and oxygen depletion in proximal shelf settings. However, this non-sulfidic state efficiently sequestered phosphorus in the sediment in association with iron minerals, thus restricting the intensity and spatial extent of oxygen-depleted waters. The collapse of vegetation on land immediately prior to the marine extinction changed the relative weathering influx of iron and sulfate. The resulting transition to euxinic (sulfidic) conditions led to enhanced remobilization of bioavailable phosphorus, initiating a feedback that caused the spread of anoxic waters across large portions of the shelf. This reconciles a lag of >0.3 My between the onset of enhanced weathering and the development of widespread, but geographically variable, ocean anoxia, with major implications for extinction selectivity.

The Permian–Triassic (P–Tr) boundary (~251.9 million years ago<sup>1</sup>) record contains multiple signals suggestive of widespread marine anoxia, a kill mechanism widely implicated in the end-Permian mass extinction<sup>2–7</sup>. This crisis was the most dramatic turning-point in the evolution of post-Cambrian life, with a loss of up to 81% of marine species<sup>8</sup>. Mechanisms for the development of oxygen-depleted oceans on timescales compatible with the duration of the extinction (~60 ky<sup>1</sup>), include changes in ocean circulation<sup>9</sup>, decreased O<sub>2</sub> solubility under globally rising temperatures<sup>10</sup>, and enhanced eutrophication<sup>10–13</sup>. In the latter case, recent studies have postulated that changes in the marine inventory of phosphorus (P)—the ultimate limiting nutrient for marine productivity on geological timescales<sup>14</sup>—was the main driver for eutrophication-induced oxygen depletion and ultimately the development of euxinic conditions in extensive regions of the global ocean<sup>10,11,13</sup>.

During Siberian Traps volcanism, an increase in bioavailable phosphorus would be an expected consequence of increased continental weathering via the dissolution of exposed rock (driven by CO<sub>2</sub>-induced warming, and SO<sub>2</sub>-induced acid rain), and the disintegration of rock by an invigorated hydrological cycle<sup>11,12,15,16</sup>. Indeed, a coeval change in both lithium (Li) concentrations and Li isotope ratios has been interpreted to reflect an increase in weathering<sup>16</sup>. Subsequently, a change in eruption style to intrusive basalt emplacement has been linked to halocarbon remobilization and exhalations leading to ozone layer depletion and consequent terrestrial plant extirpations by UV-B irradiance<sup>17,18</sup>. The effects of this intrusive volcanic phase on land-plant communities have therefore been related to reduced soil stability<sup>12,15,19</sup>. Combined with continued greenhouse-induced global warming, and associated changes in the hydrological cycle, this situation likely led to increased soil erosion and physical weathering, thereby loading near-shore environments with a higher sediment influx and terrestrial organics<sup>4,7,12,15</sup>.

Certain aspects of this scenario are problematic, as Siberian Traps activity spans >1 My, with 2/3 of the volume of lava deposited ~0.3 My before the main extinction pulse<sup>18</sup>. Furthermore, localized regions of dysoxia/anoxia occur prior to the mass extinction<sup>3,4,6</sup>, but a major expansion in the areal extent of these conditions occurred at the extinction horizon<sup>5,7</sup>. The role of these precursor environmental changes in pre-stressed communities is underexplored<sup>20</sup>, and requires knowledge of the mechanisms that drove the initiation of localized oxygen depletion and the ensuing expansion of anoxic regions.

While an increase in the oceanic influx of bioavailable phosphorus may have occurred in association with Siberian Traps activity<sup>11,16</sup>, the catalytic effect of local redox conditions on benthic phosphorus remobilization has often been overlooked in scenarios of eutrophication-induced marine anoxia. Phosphorus is delivered to sediments in the form of organic matter and skeletal remains (biogenic apatite), as well as in association with Fe (oxyhydr)oxides and recalcitrant detrital minerals<sup>21-24</sup>. Organically bound-P ( $P_{org}$ ) may be preferentially released to sediment porewaters upon microbial remineralisation, resulting in increased  $C_{org}/P_{org}$  ratios in deposited sediments<sup>21,22</sup>. In addition, the reductive dissolution of Fe (oxyhydr)oxides releases adsorbed P to solution<sup>21-23</sup>, while biogenic apatite tends to be highly soluble<sup>24</sup>.

The dissolved P generated by these processes may undergo 'sink-switching', whereby dependent on the precise conditions, dissolved P may precipitate as either carbonate-fluorapatite (CFA)<sup>25</sup> or Fe phosphates (e.g., vivianite)<sup>26</sup>, or may be readsorbed to Fe (oxyhydr)oxides where such minerals persist<sup>23</sup>. However, under sulfidic conditions in particular, a significant proportion of the dissolved P generated during early diagenesis may be recycled back to the water column, thus promoting a positive productivity feedback<sup>27</sup>. By contrast, organic-rich oxic, dysoxic and ferruginous (anoxic Fe(II)-rich) settings are potential loci of high P deposition. These features of

phosphorus cycling thus place important constraints on the bio-availability of P, and hence may ultimately control both the spread of anoxia and the generation of toxic dissolved sulfide<sup>11,27,28</sup>.

Previous attempts to reconstruct phosphorus availability<sup>13</sup> across the P–Tr transition have lacked a precise reconstruction of ocean redox conditions, and detailed consideration of the phase partitioning of P, which are essential to evaluate the role of the P recycling feedback. To address this we apply novel sedimentary P records combined with independent redox proxies to a bathymetric transect across the P–Tr boundary.

## **Geological setting and materials**

We investigated the Festningen and Deltadalen sequences (Svalbard; Fig. 1), that were deposited on a shallow, open-marine shelf at the northern margin of Pangaea, facing the Boreal Sea and the Panthalassa Ocean beyond (Supplementary Fig. 1 and Sections 1–4). The Kapp Starostin Formation consists of dark, massive to bedded spiculitic chert (with minor shale) at Festningen<sup>6,29</sup>, and glauconitic, fine-grained sandstone with chert nodules and beds at Deltadalen, where the latter is interpreted to be a comparatively more proximal facies<sup>6,30,31</sup>. The Kapp Starostin Formation is overlain by the shale-dominated Vardebukta Formation at Festningen, and, the Vikinghøgda Formation at Deltadalen.

The end-Permian mass extinction has been defined by a loss of intense bioturbation dominated by *Zoophycos*<sup>4,6</sup>. However, shallow bioturbation, dominated by small *Planolites*, persists for ~3 m above the formational contact at Festningen, before disappearing<sup>2</sup>. The P–Tr boundary is defined by the aid of the  $\delta^{13}\text{C}_{\text{org}}$  record (Fig. 2 and Supplementary Fig. 2) and the conodont marker species *Hindeodus parvus*<sup>31</sup>.

## 90    **Local redox chemistry**

91            We combined iron speciation analyses with redox-sensitive trace element concentrations  
92    (Methods) to differentiate oxic, dysoxic, anoxic ferruginous, and euxinic water column  
93    conditions<sup>32,33</sup>. The Fe speciation method relies on the quantification of operationally-defined Fe  
94    fractions that are considered highly reactive ( $\text{Fe}_{\text{HR}}$ ) towards dissolved sulfide on early diagenetic  
95    timescales<sup>34,35</sup>. The proportion of  $\text{Fe}_{\text{HR}}$  relative to total iron ( $\text{Fe}_{\text{tot}}$ ) has been extensively calibrated  
96    in modern and ancient settings, such that  $\text{Fe}_{\text{HR}}/\text{Fe}_{\text{tot}} > 0.38$  suggest an anoxic water column,  
97    values below 0.22 indicate oxic depositional conditions, and values of 0.22–0.38 are considered  
98    equivocal<sup>36</sup>. The extent of pyritisation of  $\text{Fe}_{\text{HR}}$  is used to differentiate euxinic ( $\text{Fe}_{\text{py}}/\text{Fe}_{\text{HR}} > 0.7$ –  
99    0.8) from ferruginous water column conditions ( $\text{Fe}_{\text{py}}/\text{Fe}_{\text{HR}} < 0.7$ )<sup>36</sup>.

100            Non-sulfidized  $\text{Fe}_{\text{HR}}$  has the potential to be converted to less reactive sheet silicate  
101    minerals (termed poorly reactive sheet silicate Fe;  $\text{Fe}_{\text{PRS}}$ ) during early diagenesis and deeper  
102    burial<sup>35,37,38</sup>. Depletion of  $\text{Fe}_{\text{HR}}$  by this mechanism is clearly observed in some of the studied  
103    samples, and is marked by the co-occurrence of glauconite at both localities. Glauconite occurs  
104    as fibroradiated precipitates covering quartz grains and shell fragments, suggesting an authigenic  
105    precipitate rather than a late diagenetic replacement product or detrital source, and thus  $\text{Fe}_{\text{HR}}$   
106    minerals would have been the primary source. To compensate for this transfer of  $\text{Fe}_{\text{HR}}$  to  
107    glauconite, we apply a correction to samples that show clear enrichment in  $\text{Fe}_{\text{PRS}}$  over  
108    background values, yielding estimates ( $\text{Fe}_{\text{HR}}/\text{Fe}_{\text{tot}}^*$ ,  $\text{Fe}_{\text{py}}/\text{Fe}_{\text{HR}}^*$ ) of initial depositional ratios<sup>39</sup>  
109    (Fig. 2, Supplementary Figs. 3 and 6, and Section 7.2).

110            The distinctive geochemical behaviour of molybdenum (Mo), uranium (U) and rhenium  
111    (Re) provides further insight into water column redox conditions. High sediment Mo

accumulation tends to occur when water column concentrations of sulfide are high, and likely relates to the formation of particle-reactive thiomolybdates<sup>33</sup>. By contrast, U may be fixed in the sediment under anoxic porewater conditions, without the requirement for free H<sub>2</sub>S, and Re may be sequestered under dysoxic conditions in the water column and sediments, where O<sub>2</sub> penetrates <1 cm below the sediment–water interface<sup>33,40</sup>. Therefore, high Re/Mo ratios tend to indicate dysoxic water column conditions<sup>40</sup>, whereas enhanced Mo/U ratios suggest a euxinic water column<sup>33</sup>.

The pre-extinction sandstone of the proximal Deltadalen locality is conspicuous for its authigenic glauconite content. Glauconite formation is favoured by elevated concentrations of Fe<sub>HR</sub>, silica and potassium under dysoxic conditions<sup>41,42</sup>. High Re/Mo ratios across this interval (Fig. 2)<sup>40</sup> coupled with the ichnoassemblage and the impoverished shelly faunal record, which consists of the inarticulate brachiopod *Lingularia freboldi*<sup>43,44</sup> (Supplementary Figs. 4 and 5; and Section 7.1), are consistent with prevailing dysoxic seafloor conditions. Thus, the elevated Fe<sub>HR</sub>/Fe<sub>tot</sub>\* values of the Kapp Starostin Formation (Fig. 2) likely reflect the influx of a high proportion of Fe (oxyhydr)oxides produced during enhanced weathering<sup>35</sup>, rather than anoxic water column conditions.

Enrichments in Re begin to decrease below the extinction interval at Deltadalen, coincident with increasing Mo/U ratios (Fig. 2). These high ratios coincide with enhanced fixation of Fe<sub>HR</sub> as pyrite (Fig. 2), Mo<sub>EF</sub>–U<sub>EF</sub> that approach those observed in modern euxinic settings (Fig. 3), and the disappearance of burrows (Supplementary Fig. 2), suggesting the development of dominantly euxinic conditions in the water column in proximal settings at the extinction boundary and into the Early Triassic<sup>33,36</sup>



The sponge spiculite chert of the Kapp Starostin Formation at Festningen (distal) is marked by  $\text{Fe}_{\text{HR}}/\text{Fe}_{\text{tot}}^*$  values in the equivocal zone, as well as low Mo/U and generally low Re/Mo (Fig. 2). These vast sponge meadows are consistent with a well-oxygenated water column<sup>30</sup>, whereas infrequent peaks in Re/Mo may indicate occasional dysoxic conditions. A pronounced peak in non-sulfidized iron, coincident with enrichments in  $\text{Fe}_{\text{HR}}$ , the precipitation of glauconite, muted Re/Mo enrichments and bioturbation intensity (Supplementary Fig. 2), occurs at the extinction horizon in the basal Vardebukta Formation (Fig. 2), suggesting the development of dysoxic and/or ferruginous conditions in the water column. Enrichments in  $\text{Fe}_{\text{HR}}$  persist across the P–Tr boundary at ~5 m above the base of the Vardebukta Formation, with elevated  $\text{Fe}_{\text{py}}/\text{Fe}_{\text{HR}}^*$ , moderate enrichments in Mo relative to U (Fig. 2), the cessation of bioturbation (Supplementary Fig. 2), and  $\text{Mo}_{\text{EF}}\text{--}\text{U}_{\text{EF}}$  that are comparable to normal oxic marine settings (Fig. 3). Together, this implies the probable development of water column euxinia, but relatively low levels of Mo drawdown imply either intermittent or weakly sulfidic conditions in this more distal setting<sup>46</sup>.

The spatio-temporal variability in water column redox implies the existence of dysoxic conditions on the shallow shelf prior to the extinction (Fig. 2). Subsequently, at the extinction horizon, euxinic conditions developed at the shallowest location (Deltadalen), and dysoxic to ferruginous conditions expanded into more distal shelf settings (Festningen). This was followed by the expansion of anoxia across the shelf, with euxinic conditions becoming more widespread in the post-extinction Early Triassic. The S isotope composition of pyrite provides additional support for this redox reconstruction. Generally low and quite variable pyrite  $\delta^{34}\text{S}$  values ( $-32.7 \pm 9.9\text{‰}$ ) prior to the extinction horizon at the more distal locality (Fig. 2) are consistent with microbial sulfate reduction in sediments deposited beneath an oxic water column<sup>47</sup>. By contrast,

high  $\delta^{34}\text{S}_{\text{py}}$  where glauconite is prevalent, both in the lower section of the more proximal locality (-16.7  $\pm$  12.1‰) and just above the extinction horizon at the more distal locality (-16.8  $\pm$  15.1‰), suggests more complete consumption of sulfate, possibly linked to temporal and spatial variability in sulfate concentrations across the transect. Particularly in the case of the distal glauconite-rich horizon, relatively high  $\delta^{34}\text{S}_{\text{py}}$  may be due to significant drawdown of the continental sulfate flux under euxinic conditions on the more proximal shelf. However, under euxinic conditions at both sites,  $\delta^{34}\text{S}_{\text{py}}$  values cluster around a narrow range (-27.8  $\pm$  5.4‰), which is consistent with the narrow range commonly found in modern and ancient euxinic settings<sup>47,48</sup>.

We use our phosphorus data to test two scenarios that are compatible with redox change at the extinction horizon. Firstly, the  $\text{Fe}_{\text{HR}}$  flux from the continent may have dropped (Fig. 2) proportional to the sulfate influx with the switch to deforestation, soil erosion and increased physical weathering<sup>12,15,16,19</sup>. Alternatively, an increase in organic carbon ( $\text{C}_{\text{org}}$ ) availability (Fig. 4) under eutrophic conditions on the shelf may have increased the production of  $\text{H}_2\text{S}$ , thus overwhelming the continental supply of  $\text{Fe}_{\text{HR}}$ . Both of these scenarios would initially promote enhanced production of sulfide on the more proximal continental shelf.

## **Phosphorus recycling and the spread of anoxia**

To assess the potential role of phosphorus in driving our proposed redox structure we quantified different phosphorus-bearing phases (Methods), specifically Fe (oxyhydr)oxide-bound P ( $\text{P}_{\text{Fe}}$ ), biogenic and authigenic apatite ( $\text{P}_{\text{aut}}$ ), organic-P ( $\text{P}_{\text{org}}$ ), and crystalline detrital phases ( $\text{P}_{\text{det}}$ )<sup>25</sup>. While detrital P is generally considered unreactive in the water column and during early diagenesis, the remaining phases comprise a ‘reactive’ P pool ( $\text{P}_{\text{reac}}$ ). However, Fe(III)-rich sheet

silicates (e.g. glauconite) can also effectively trap phosphate<sup>49</sup>, which is extracted as part of the  $P_{\text{det}}$  pool (Supplementary Fig. 7 and Section 7.3).

Prior to the extinction at Deltadalen (proximal),  $P_{\text{tot}}/\text{Al}$  is considerably enriched relative to average marine shale (Fig. 4). This suggests an effective drawdown mechanism from a water column that was rich in phosphate. Furthermore, although preferential release from organic matter occurred during diagenesis ( $C_{\text{org}}/P_{\text{org}} >$  the molar Redfield ratio of 106/1), low  $C_{\text{org}}/P_{\text{reac}}$  ratios ( $\ll 106/1$ ) combined with high  $P_{\text{tot}}/\text{Al}$ , suggest effective sequestration of P in the sediment, with no evidence for extensive recycling. To explain these observations we invoke a high initial weathering influx of phosphate to the proximal shelf associated with initial emplacement of the Siberian Traps prior to the extinction<sup>18</sup>, which enhanced productivity and  $C_{\text{org}}$  remineralisation in the water column, leading to the development of dysoxic conditions (Fig. 5). However, the extent and intensity of deoxygenation was limited by effective drawdown of P to the sediments in association with both  $C_{\text{org}}$  and the high weathering influx of Fe (oxyhydr)oxide minerals, and with long-term retention in CFA and glauconite (Supplementary Fig. 7).

These factors then controlled the geochemistry prior to the extinction at Festningen (distal), where  $P_{\text{tot}}/\text{Al}$  ratios are close to average shale,  $C_{\text{org}}/P_{\text{org}}$  ratios are elevated relative to the Redfield ratio, and  $C_{\text{org}}/P_{\text{reac}}$  ratios scatter close to the Redfield ratio (Fig. 4). This suggests that the high initial weathering influx of P was efficiently sequestered in more proximal settings, thus limiting the spatial extent of dysoxic conditions. Furthermore, while P was released from organic matter during microbial respiration ( $C_{\text{org}}/P_{\text{org}} > 106/1$ ), there is little evidence for a high sustained flux back to the water column ( $C_{\text{org}}/P_{\text{reac}} \approx 106$ ), consistent with the expected behaviour of P in sediments deposited beneath an oxic water column<sup>27,28</sup>.

At the extinction horizon,  $P_{\text{tot}}/\text{Al}$  ratios decrease to average shale values at Deltadalen (proximal), and both  $C_{\text{org}}/P_{\text{org}}$  and  $C_{\text{org}}/P_{\text{reac}}$  ratios increase considerably to values that exceed the Redfield ratio (Fig. 4). This suggests that the development of euxinia fuelled efficient release of P from both  $C_{\text{org}}$  and Fe (oxyhydr)oxides, and a positive productivity feedback was promoted via enhanced P recycling. The initial driver of euxinia is more difficult to ascertain, but was likely related to the change to a chemical weathering-limited denudation regime<sup>19</sup> (Fig. 2), thereby decreasing the land-derived influx of  $\text{Fe}_{\text{HR}}$ . This led to a tipping point whereby a relative excess of dissolved sulfate over  $\text{Fe}_{\text{HR}}$  promoted the development of euxinia<sup>36</sup>. As discussed above, an increase in eutrophication driven by an enhanced nutrient influx may also have promoted sulfide production. However, this seems a less likely explanation for the initial driver of euxinia given the already high input of P (Fig. 4).

In glauconite-rich sediments immediately above the extinction horizon at Festningen (distal), there is an initial peak in  $P_{\text{tot}}/\text{Al}$  in association with the development of dysoxic and/or ferruginous conditions. Here, our detailed P speciation analyses suggest that, as with the glauconite-rich horizon in the proximal locality, P was trapped in the sediment in association with CFA and glauconite (Supplementary Fig. 7). The high P content of this horizon likely occurred due to drawdown of P that was recycled under euxinic conditions in more proximal settings, suggesting the operation of a redox-controlled nutrient shuttle across the shelf. This nutrient shuttle then drove the development of marine euxinia to its maximum extent in the aftermath of the mass extinction (Fig. 5), where wind/density-driven water circulation on the shelf would support upward transport of recycled P, and thus sustained deoxygenation<sup>11</sup>. At Festningen, however, the development of only weak or intermittent euxinia after the P–Tr

boundary restricted the extent of P recycling to the water column ( $C_{\text{org}}/P_{\text{reac}} \approx 106/1$ ; Fig. 4), which effectively constrained the maximum spatial extent of euxinia.

## **Implications for extinction selectivity**

This P-driven biogeochemical cascade is synchronous with independent proxy records for the global-scale spread of anoxic water masses<sup>5,7</sup>, and it was this that initiated the main marine extinction pulse. The P-driven control on the extent of initial deoxygenation and subsequent euxinia promoted life-viable environments in the deep marine realm, thereby shaping the ecosystems of the surviving biota. Based on the benthos that survived the end-Permian mass extinction at Deltadalen, a planktotrophic larval stage<sup>50</sup> (Supplementary Section 7.1) and a high-tolerance to low-oxygen conditions are important traits. These benthic species could rapidly disperse over large distances, thus increasing the chance of survival in habitable locations.

In accordance with theoretical ecological models<sup>51</sup>, environmental deterioration of the marine realm began before the extinction pulse. The initial development of dysoxic/anoxic water masses, which were preferentially situated in shallow marine environments in the Boreal region<sup>20</sup>, may thus be regarded as a prelude to the impending mass extinction. Our redox model also resolves the apparent conflict between the timing of magmatic activity<sup>18</sup>, enhanced weathering<sup>16</sup>, and the main extinction pulse. The sum of these changes in marine redox conditions across large stretches of the shelf, which harboured the majority of the Palaeozoic biodiversity<sup>2</sup>, appears to have been detrimental to many life forms at the end of the Permian.

## References

1. Burgess, S. D., Bowring, S. & Shen, S.-z. High-precision timeline for Earth's most severe extinction. *P. Natl. Acad. Sci. Usa.* **111**, 3316–3321 (2014).
2. Wignall, P. B. & Twitchett, R. J. Oceanic anoxia and the End Permian mass extinction. *Science* **272**, 1155–1158 (1996).
3. Cao, C. *et al.* Biogeochemical evidence for euxinic oceans and ecological disturbance presaging the end-Permian mass extinction event. *Earth Planet. Sc. Lett.* **281**, 188–201 (2009).
4. Nabbefeld, B. *et al.* An integrated biomarker, isotopic and palaeoenvironmental study through the Late Permian event at Lusitaniadalen, Spitsbergen. *Earth Planet. Sc. Lett.* **291**, 84–96 (2010).
5. Brennecka, G. a., Herrmann, a. D., Anbar, a. D. & Algeo, T. J. Rapid expansion of oceanic anoxia immediately before the end-Permian mass extinction. *P. Natl. Acad. Sci. Usa.* **108**, 17631–17634 (2011).
6. Dustira, A. M. *et al.* Gradual onset of anoxia across the Permian-Triassic Boundary in Svalbard, Norway. *Palaeogeogr. Palaeoclimatol. Palaeoecol.* **374**, 303–313 (2013).
7. Schobben, M. *et al.* Flourishing ocean drives the end-Permian marine mass extinction. *P. Natl. Acad. Sci. Usa.* **112**, 10298–10303 (2015).
8. Stanley, S. M. Estimates of the magnitudes of major marine mass extinctions in earth history. *P. Natl. Acad. Sci. Usa.* **113**, E6325–E6334 (2016).

- 264 9. Kiehl, J. T. & Shields, C. A. Climate simulation of the latest Permian: Implications for mass  
265 extinction. *Geology* **33**, 757–760 (2005).
- 266 10. Hotinski, R. M., Bice, K. L., Kump, L. R., Najjar, R. G. & Arthur, M. A. Ocean stagnation  
267 and end-Permian anoxia. *Geology* **29**, 7–10 (2001).
- 268 11. Meyer, K., Kump, L. & Ridgwell, A. Biogeochemical controls on photic-zone euxinia during  
269 the end-Permian mass extinction. *Geology* **36**, 747 (2008).
- 270 12. Algeo, T. J. & Twitchett, R. J. Anomalous Early Triassic sediment fluxes due to elevated  
271 weathering rates and their biological consequences. *Geology* **38**, 1023–1026 (2010).
- 272 13. Shen, J. *et al.* Marine productivity changes during the end-Permian crisis and Early Triassic  
273 recovery. *Earth-sci. Rev.* **149**, 136–162 (2015).
- 274 14. Tyrrell, T. The relative influences of nitrogen and phosphorus on oceanic primary  
275 production. *Nature* **400**, 525–531 (1999).
- 276 15. Sephton, M. a. *et al.* Catastrophic soil erosion during the end-Permian biotic crisis. *Geology*  
277 **33**, 941–944 (2005).
- 278 16. Sun, H. *et al.* Rapid enhancement of chemical weathering recorded by extremely light  
279 seawater lithium isotopes at the Permian–Triassic boundary. *P. Natl. Acad. Sci. Usa.* **115**,  
280 3782–3787 | (2018).
- 281 17. Visscher, H. *et al.* Environmental mutagenesis during the end-Permian ecological crisis. *P.*  
282 *Natl. Acad. Sci. Usa.* **101**, 12952–12956 (2004).
- 283 18. Burgess, S. D., Muirhead, J. D. & Bowring, S. A. Initial pulse of Siberian Traps sills as the  
284 trigger of the end-Permian mass extinction. *Nat. Commun.* **8**, 1–4 (2017).

- 285 19. Ward, P. D., Montgomery, D. R. & Smith, R. Altered river morphology in South Africa  
286 related to the Permian-Triassic extinction. *Science* **289**, 1740–1743 (2000).
- 287 20. Algeo, T. *et al.* Evidence for a diachronous Late Permian marine crisis from the Canadian  
288 Arctic region. *Geol. Soc. Am. Bull.* **124**, 1424–1448 (2012).
- 289 21. Froelich, P. N. *et al.* Early oxidation of organic matter in pelagic sediments of the eastern  
290 equatorial Atlantic: suboxic diagenesis. *Geochim. Cosmochim. Ac.* **43**, 1075–1090  
291 (1979).
- 292 22. Krom, M. D. & Berner, R. A. The diagenesis of phosphorus in a nearshore marine sediment.  
293 *Geochim. Cosmochim. Ac.* **45**, 207–216 (1981).
- 294 23. Slomp, C. P., Van Der Gaast, S. J. & Van Raaphorst, W. Phosphorus binding by poorly  
295 crystalline iron oxides in North Sea sediments. *Mar. Chem.* **52**, 55–73 (1996).
- 296 24. Schenau, S. J. & De Lange, G. J. A novel chemical method to quantify fish debris in marine  
297 sediments. *Limnol. Oceanogr.* **45**, 963–971 (2000).
- 298 25. Ruttenberg, K. C. Development of a sequential extraction method for different forms of  
299 phosphorus in marine sediments. *Limnol. Oceanogr.* **37**, 1460–1482 (1992).
- 300 26. Egger, M., Jilbert, T., Behrends, T., Rivard, C. & Slomp, C. P. Vivianite is a major sink for  
301 phosphorus in methanogenic coastal surface sediments. *Geochim. Cosmochim. Ac.* **169**,  
302 217–235 (2015).
- 303 27. Cappellen, P. V. & Ingall, E. D. Redox Stabilization of the Atmosphere and Oceans by  
304 Phosphorus-Limited Marine Productivity. *Science* **271**, 493–496 (1996).



- 305 28. Algeo, T. J. & Ingall, E. Sedimentary Corg:P ratios, paleocean ventilation, and Phanerozoic  
306 atmospheric pO<sub>2</sub>. *Palaeogeogr. Palaeoclimatol. Palaeoecol.* **256**, 130–155 (2007).
- 307 29. Harland, W. *The geology of Svalbard*. 521 (Geological Society Memoir No.17, 1997).
- 308 30. Blomeier, D., Dustira, A. M., Forke, H. & Scheibner, C. Facies analysis and depositional  
309 environments of a storm-dominated, temperate to cold, mixed siliceous–carbonate ramp:  
310 the Permian Kapp Starostin Formation in NE Svalbard. *Norw. J. Geol.* **93**, 75–93 (2013).
- 311 31. Zuchuat, V. *et al.* A new high-resolution stratigraphic and palaeoenvironmental record  
312 spanning the End-Permian Mass Extinction and its aftermath in central Spitsbergen,  
313 Svalbard. *Palaeogeogr. Palaeoclimatol. Palaeoecol.* 109732 (2020)  
314 doi:[10.1016/j.palaeo.2020.109732](https://doi.org/10.1016/j.palaeo.2020.109732).
- 315 32. Poulton, S. W. & Canfield, D. E. Development of a sequential extraction procedure for iron:  
316 Implications for iron partitioning in continentally derived particulates. *Chem. Geol.* **214**,  
317 209–221 (2005).
- 318 33. Algeo, T. & Tribovillard, N. Environmental analysis of paleoceanographic systems based on  
319 molybdenum–uranium covariation. *Chem. Geol.* **268**, 211–225 (2009).
- 320 34. Raiswell, R. & Canfield, D. E. Sources of iron for pyrite formation in marine sediments. *Am.*  
321 *J. Sci.* **298**, 219–245 (1998).
- 322 35. Poulton, S. W. & Raiswell, R. The low-temperature geochemical cycle of iron: From  
323 continental fluxes to marine sediment deposition. *Am. J. Sci.* **302**, 774–805 (2002).
- 324 36. Poulton, S. W. & Canfield, D. E. Ferruginous conditions: A dominant feature of the ocean  
325 through Earth’s history. *Elements* **7**, 107–112 (2011).

- 326 37. Lyons, T. W. & Severmann, S. A critical look at iron paleoredox proxies: New insights from  
327 modern euxinic marine basins. *Geochim. Cosmochim. Ac.* **70**, 5698–5722 (2006).
- 328 38. Poulton, S. W., Fralick, P. W. & Canfield, D. E. Spatial variability in oceanic redox structure  
329 1.8 billion years ago. *Nat. Geosci.* **3**, 486–490 (2010).
- 330 39. Doyle, K. A., Poulton, S. W., Newton, R. J., Podkovyrov, V. N. & Bekker, A. Shallow water  
331 anoxia in the Mesoproterozoic ocean: Evidence from the Bashkir Meganticlinorium,  
332 Southern Urals. *Precambrian Res.* **317**, 196–210 (2018).
- 333 40. Kendall, B. *et al.* Pervasive oxygenation along late Archaean ocean margins. *Nat. Geosci.* **3**,  
334 647–652 (2010).
- 335 41. Chafetz, H. S. & Reid, A. Syndepositional shallow-water precipitation of glauconitic  
336 minerals. *Sediment. Geol.* **136**, 29–42 (2000).
- 337 42. Peters, S. E. & Gaines, R. R. Formation of the 'Great Unconformity' as a trigger for the  
338 Cambrian explosion. *Nature* **484**, 363–366 (2012).
- 339 43. Manwell, C. Oxygen Equilibrium of Brachiopod *Lingula Hemerythrin*. *Science* **132**, 550–551  
340 (1960).
- 341 44. Peng, Y., Shi, G. R., Gao, Y., He, W. & Shen, S. How and why did the Lingulidae  
342 (Brachiopoda) not only survive the end-Permian mass extinction but also thrive in its  
343 aftermath? *Palaeogeogr. Palaeoclimatol. Palaeoecol.* **252**, 118–131 (2007).
- 344 45. Wedepohl, K. H. The composition of the upper earth's crust and the natural cycles of  
345 selected metals. Metals in natural raw materials. Natural Resources. in *Metals and their*  
346 *compounds in the environment* (ed. Merian, E.) 3–17 (Verlag Chemie, 1991).

46. Scott, C. & Lyons, T. W. Contrasting molybdenum cycling and isotopic properties in euxinic versus non-euxinic sediments and sedimentary rocks: Refining the paleoproxies. *Chem. Geol.* **324-325**, 19–27 (2012).
47. Lyons, T. W. Sulfur isotopic trends and pathways of iron sulfide formation in upper Holocene sediments of the anoxic Black Sea. *Geochim. Cosmochim. Ac.* **61**, 3367–3382 (1997).
48. Shen, Y., Canfield, D. E. & Knoll, A. H. Middle proterozoic ocean chemistry: Evidence from the McArthur Basin, Northern Australia. *Am. J. Sci.* **302**, 81–109 (2002).
49. Borgnino, L., Avena, M. & De Pauli, C. Synthesis and characterization of Fe(III)-montmorillonites for phosphate adsorption. *Colloid. Surface. A.* **341**, 46–52 (2009).
50. Foster, W. J., Danise, S. & Twitchett, R. J. A silicified Early Triassic marine assemblage from Svalbard. *J. Syst. Palaeontol.* **15**, 851–877 (2017).
51. Barnosky, A. D. *et al.* Approaching a state shift in Earth’s biosphere. *Nature* **486**, 52–8 (2012).

## Correspondence

Correspondence should be addressed to MS (m.a.n.schobben@uu.nl). PBW (P.B.Wignall@leeds.ac.uk) and SP (planke@vbpr.no) should be consulted for material requests of Festningen and Deltadalen, respectively.

## **Acknowledgements**

MS was funded by a DFG Research Fellowship (SCHO 1689/1–1). SWP acknowledges support from a Royal Society Wolfson Research Merit Award and a Leverhulme Research Fellowship. DPGB acknowledges funding from the Natural Environment Research Council (NE/J01799X/1) as do PBW and RJN (NE/P013724/1). HHS and SP acknowledge support from the Norwegian Research Council by Centres of Excellence funding to CEED (project number 223272), and Lundin Petroleum, Arctic Drilling AS and Store Norske Spitsbergen Kulkompani for funding, drilling, and support related to the Deltadalen core.

## **Author contributions**

The study was designed by MS, RJN, PBW and SWP. Samples were collected by VZ, ARNS, HS, SP, PBW, and DPGB. Palaeontological data acquisition was performed by WJF, MS, PBW, and DPGB. Geochemical analyses were performed by MS, FM and RJN. MS and SWP interpreted data. MS led the writing of the manuscript with contributions from all co-authors.

## **Competing interests**

The authors declare no competing interests.

## **Figure captions**

**Figure 1: Geographical setting of the Festningen section (1) and Deltadalen core (2).** Late Permian lithofacies of Spitsbergen after ref 29 and Supplementary Section 2; the tentative location of a northern source area (possibly on the Nordfjorden High) demarcated with a

question mark; and the Sørkapp-Hornsund High encircled with a dotted line. The red dots mark the exact locations of the sites. Base map from GADM database (<https://gadm.org/>)

**Figure 2: Stratigraphic plot of  $\delta^{13}\text{C}_{\text{org}}$ , Fe speciation, Mo/U, Re/Mo and  $\delta^{34}\text{S}_{\text{py}}$  for the Festningen outcrop and Deltadalen core.** The boundaries (vertical dotted lines) for oxic, anoxic, ferruginous (Fe(II)-rich) and euxinic ( $\text{H}_2\text{S}$ -rich) water column conditions were calibrated in modern and ancient aquatic environments (see text for sources). Iron speciation ( $\text{Fe}_{\text{py}}/\text{Fe}_{\text{HR}}^*$ ,  $\text{Fe}_{\text{HR}}/\text{Fe}_{\text{tot}}^*$ ) corrected for excess  $\text{Fe}_{\text{PRS}}$  (excess  $\text{Fe}_{\text{PRS}} = [\text{measured } \text{Fe}_{\text{PRS}}/\text{Fe}_{\text{tot}} - \text{baseline } \text{Fe}_{\text{PRS}}/\text{Fe}_{\text{tot}}] \times \text{Fe}_{\text{tot}}$  if measured  $\text{Fe}_{\text{PRS}}/\text{Fe}_{\text{tot}} > \text{baseline } \text{Fe}_{\text{PRS}}/\text{Fe}_{\text{tot}}$ ) is shown as black circles; uncorrected values are shown as open circles (See Supplementary Section 7.2). Subscripts of isotope ratios; org = total organic matter and py = pyrite.  $\text{Fe}_{\text{py}}$  = iron pyrite;  $\text{Fe}_{\text{HR}}$  = highly reactive iron ( $\text{Fe}_{\text{carb}}$  [iron bound to carbonate] +  $\text{Fe}_{\text{ox}}$  [iron bound to Fe oxy(hydr)oxides] +  $\text{Fe}_{\text{mag}}$  [iron bound as magnetite] +  $\text{Fe}_{\text{py}}$ );  $\text{Fe}_{\text{tot}}$  = total iron;  $\text{Fe}_{\text{PRS}}$  = poorly reactive sheet silicate iron. Reproducibility for  $\text{Fe}_{\text{py}}$  and  $\text{Fe}_{\text{HR}}$  is better than 5% and 9% relative standard deviations (RSD), better than 8% RSD for total elemental concentrations, and better than 0.1‰ and 0.9‰ SD for  $\delta^{13}\text{C}_{\text{org}}$  and  $\delta^{34}\text{S}_{\text{py}}$ . Horizontal dashed grey line: extinction event; solid grey line: Permian–Triassic boundary. Details on lithology and stratigraphy in Supplementary Fig. 2 and Sections 2 and 3.

**Figure 3: Crossplots of Mo–U covariation.** Mo and U are given as enrichment factors ( $\text{EF} = [\text{element}/\text{Al}]_{\text{sample}}/[\text{element}/\text{Al}]_{\text{AV}}$ , where AV represents average shale<sup>45</sup>) on a  $\log_{10}$ -scale. The black dashed lines represent seawater (sw) Mo–U mass ratios for modern environments; high

(sulfidic Cariaco Basin), moderate (non-sulfidic open marine), and low (restricted, sulfidic Black Sea)<sup>33</sup>. The panels present the data of: a) Deltadalen, b) Festningen, and c) a conceptual model to explain the enrichment patterns and changes in sedimentary  $Mo_{EF}$  and  $U_{EF}$  at both sites in relation to hydrographic and redox conditions<sup>33</sup>. The solid red lines denoted by “particulate shuttle” show systematics underlain by a fluctuating chemocline, whereas “redox variation” pertains to the evolution of water mass chemistry. Note, that the red dashed line sketches the trajectory of the open marine conditions of Deltadalen from dysoxic (low Mo–high U) to euxinic (high Mo–low U).  $Fe_{py}$  = pyrite iron and  $Fe_{HR}$  = highly reactive iron.

**Figure 4: Stratigraphic distribution of  $P_{tot}/Al$ ,  $C_{org}$ ,  $C_{org}/P_{org}$ , and  $C_{org}/P_{reac}$  ratios.** The threshold of  $P_{tot}/Al$  (mass ratio of 0.008; vertical red line) is the average shale reference value<sup>45</sup>, whereas the C/P molar ratio of 106/1 denotes the Redfield ratio (vertical blue line), and the red circle represents an outlier ( $P_{tot}/Al > 2.0$ ).  $C_{org}$  = total organic matter;  $P_{org}$  = organic-bound phosphorus;  $P_{reac}$  = reactive phosphorus ( $P_{org} + P_{aut}$  [apatite P] +  $P_{Fe}$  [Fe (oxyhydr)oxide-bound P]), and  $P_{tot}$  = total phosphorus. External reproducibility for total P and Al is better than 8% RSD, better than 10% RSD for  $C_{org}$ , and better than 23% RSD for the different P phases. Horizontal dashed grey line: extinction event; solid grey line: Permian–Triassic boundary. Details on lithology and stratigraphy in Supplementary Fig. 2 and Sections 2 and 3.

**Figure 5: Conceptual model of the development of water column redox conditions.** In the Late Permian, the inner shelf was dysoxic (demarcated with  $<[O_2]$ ) and large amounts of reactive P accumulated, whereas the outer shelf harboured a thriving ecosystem (here depicted as crinoids and molluscs, but which are not representative of the actual fossil assemblages). During the end-

Permian mass extinction euxinia (demarcated with [H<sub>2</sub>S]) developed on the inner shelf, whereas the outer shelf environment became dysoxic/ferruginous (demarcated with [Fe(II)]). Under these conditions, P was remobilized as dissolved P (demarcated with H<sub>3</sub>PO<sub>4</sub>) from the inner shelf, invigorating productivity (and thus oxygen depletion), and dissolved P was recycled to the outer shelf and initially deposited through uptake by Fe (oxyhydr)oxide particles settling on the seabed. After the extinction, euxinic conditions became more prevalent across the shelf, which was initiated and maintained by recycling of P. Fe<sub>HR</sub> represents highly reactive iron.

## Methods

**Organic carbon content and carbon isotopes.** Carbonate was removed by treating the sample with 2 M HCl. The residues were repeatedly washed with MilliQ water<sup>TM</sup> and dried at 40 °C. The de-carbonated samples were analyzed for total organic carbon (TOC = C<sub>org</sub>) content and associated carbon isotopic composition using an Elementar Pyrocube elemental analyser linked to an Isoprime mass spectrometer following a standard protocol. Details regarding the reproducibility of the carbon isotope measurements and an extended protocol are included in the Supplementary Section 6.2.

**Bulk element content.** Whole rock major- (Fe, P, Al) and minor (Mo, U, Re) elements were obtained by dissolving ashed samples (550 °C over night) with HNO<sub>3</sub>–HF–HClO<sub>4</sub> followed by inductively coupled plasma optical emission spectrometry (ICP-OES). The precision of elemental analysis was monitored by analyzing certified standards, and repeated measurement yielded RSDs that are better than 8 % for all elements (Supplementary Section 6.1 and Table 1).

**Sequential Fe and P extractions.** A standard sequential Fe extraction was followed<sup>32</sup>. A sodium acetate solution at pH 4.5 for 48 h at 50 °C was used to extract Fe<sub>carb</sub>, followed by a 2 h,

room temperature extraction with sodium dithionite solution at pH 4.8 to obtain  $\text{Fe}_{\text{ox}}$ . An extraction with ammonium oxalate for 6 h at room temperature was then applied to yield  $\text{Fe}_{\text{mag}}$ . Iron from poorly reactive sheet silicates ( $\text{Fe}_{\text{PRS}}$ ) was dissolved using concentrated, boiling HCl for 1 min<sup>32</sup>. Iron concentrations in the extraction solutions were measured via atomic absorption spectrometry (AAS). Phosphorus phases were extracted via a revised SEDEX scheme for ancient rocks<sup>25,52</sup>.  $\text{P}_{\text{Fe1}}$  (poorly crystalline Fe (oxyhydr)oxides) was extracted with a sodium dithionite solution (buffered with bicarbonate to pH of 7.6) for 8 h at room temperature;  $\text{P}_{\text{aut}}$  was extracted with a sodium acetate solution at pH 4 for 6 h at room temperature;  $\text{P}_{\text{det}}$  was extracted with a 10 % HCl solution for 16 h at room temperature;  $\text{P}_{\text{mag}}$  was extracted with an ammonium oxalate solution for 6 h at room temperature;  $\text{P}_{\text{Fe2}}$  (more crystalline Fe (oxyhydr)oxides) was extracted with a sodium dithionite solution (buffered with citrate to a pH of 4.8) for 8 h at room temperature, and, finally the residue was ashed (550 °C for 2 h) and reacted with 10 % HCl solution for 16 h at room temperature to liberate  $\text{P}_{\text{org}}$ . The sum of  $\text{P}_{\text{Fe1}} + \text{P}_{\text{Fe2}} + \text{P}_{\text{mag}}$  gives  $\text{P}_{\text{Fe}}$ . The P content of the various extracts was determined either via the molybdate blue method<sup>25</sup> or ICP-OES (in the case of  $\text{P}_{\text{Fe1}}$ ,  $\text{P}_{\text{Fe2}}$  and  $\text{P}_{\text{mag}}$ ). The precision of the various Fe and P phase measurements as well as the extended protocols are reported in Supplementary Section 6.1 and Tables 2 and 3.

**Pyrite content and sulfur isotopes.** Pyrite S was measured via the chromium reduction method<sup>53</sup>. This method liberates  $\text{H}_2\text{S}$ , which is subsequently trapped as silver-sulfide ( $\text{Ag}_2\text{S}$ ). Pyrite iron was determined stoichiometrically from the weight of the  $\text{Ag}_2\text{S}$  recovered. The  $\text{Ag}_2\text{S}$  was analysed for S isotope composition using an Elementar Pyrocube linked to an Isoprime mass spectrometer (see Supplementary Section 6.2 for reproducibility of S isotope measurements and an extended protocol).



## **Data Availability**

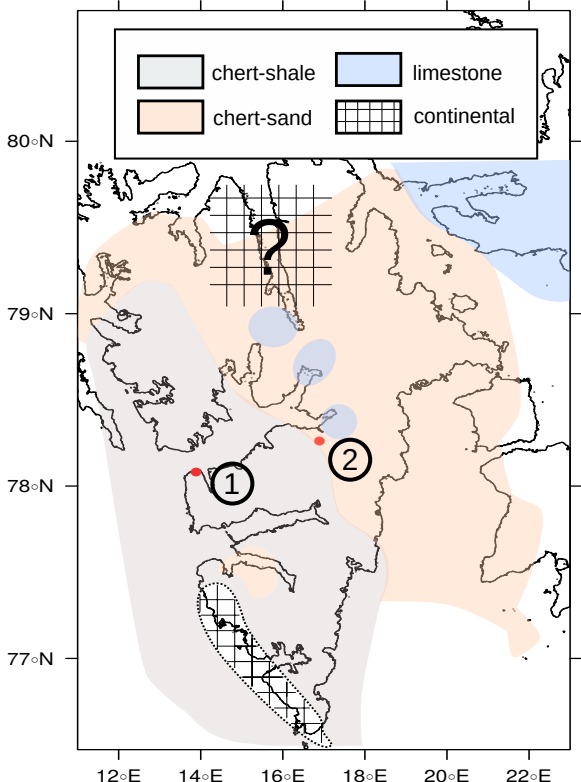
The raw and processed geochemical data that support the findings of this study are available under Zenodo: <https://doi.org/10.5281/zenodo.3878094>

## **Code Availability**

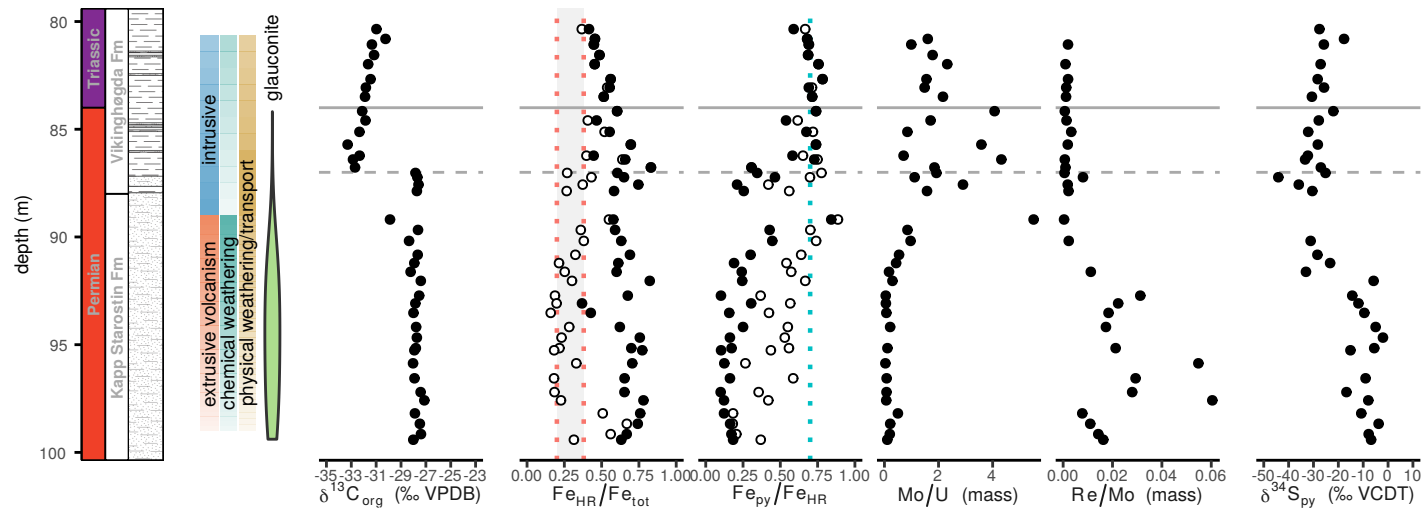
The R Markdown files to reproduce the data analysis as well as generating the accompanying data figures and the main and supplementary information texts can be found under Zenodo: <https://doi.org/10.5281/zenodo.3878094>

52. Thompson, J. *et al.* Development of a modified SEDEX phosphorus speciation method for ancient rocks and modern iron-rich sediments. *Chem. Geol.* **524**, 383–393 (2019).

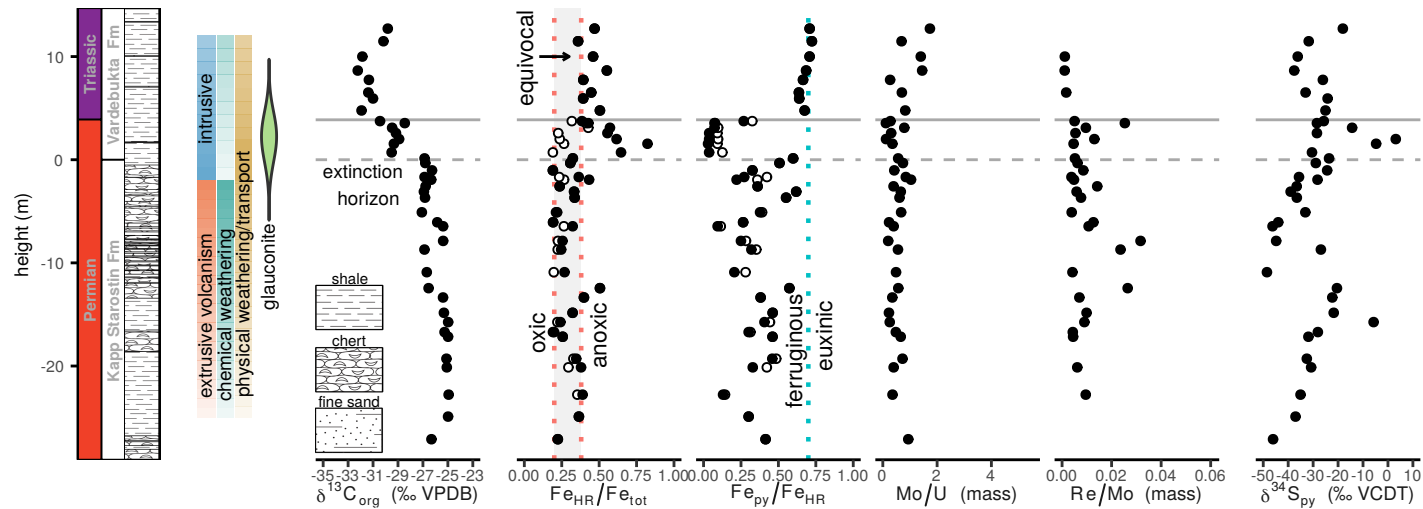
53. Canfield, D. E., Raiswell, R., Westrich, J. T., Reaves, C. M. & Berner, R. a. The use of chromium reduction in the analysis of reduced inorganic sulfur in sediments and shales. *Chem. Geol.* **54**, 149–155 (1986).



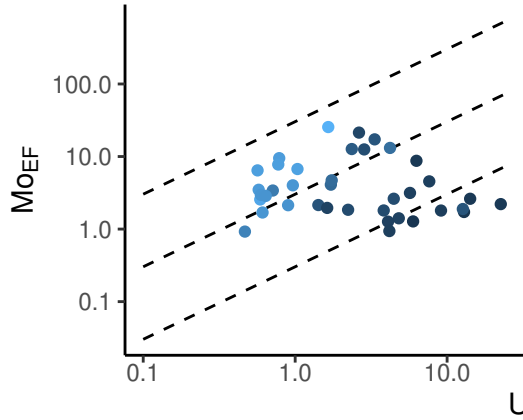
## Deltadalen (proximal)



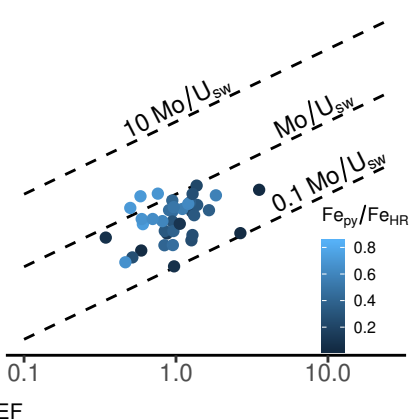
## Festningen (distal)



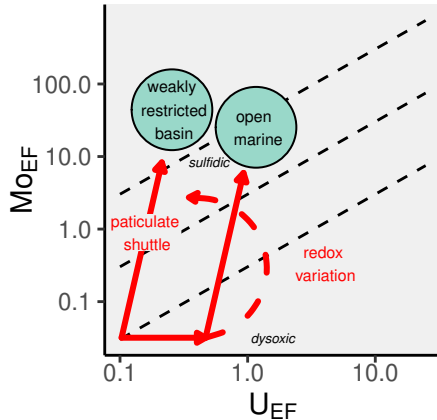
a) Deltadalen (proximal)



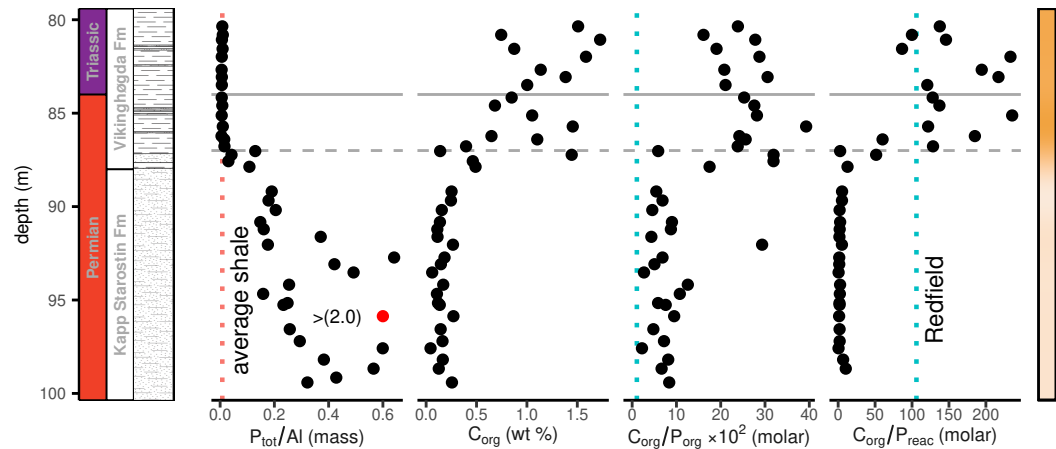
b) Festningen (distal)



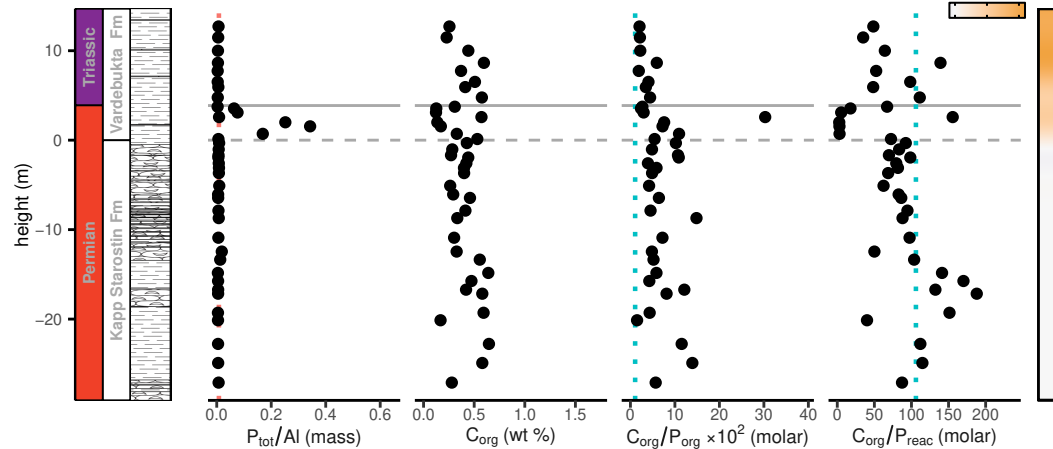
c) Model

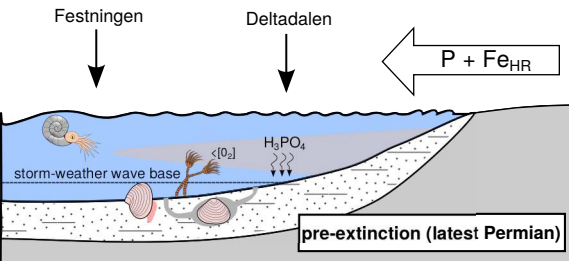
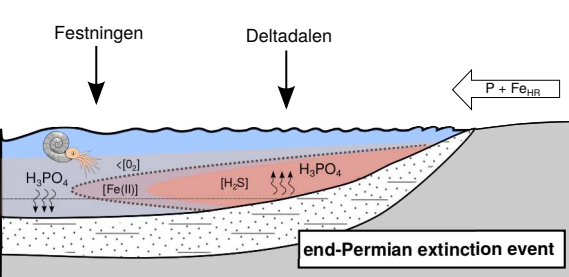
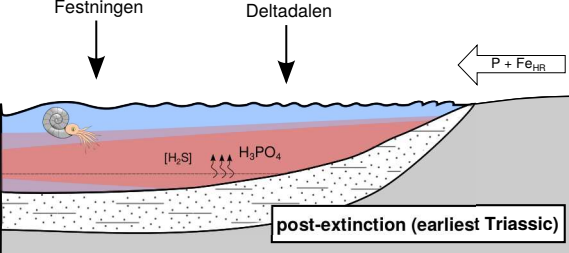


## Deltadalen (proximal)



## Festningen (distal)





younger

older

continental shelf

Nordfjorden Block